

Article

Application of a $\sqrt{\text{area}}$ -Approach for Fatigue Assessment of Cast Aluminum Alloys at Elevated Temperature

Roman Aigner ^{1,*} , Christian Garb ², Martin Leitner ¹ , Michael Stoschka ¹  and Florian Grün ² 

¹ Christian Doppler Laboratory for Manufacturing Process based Component Design, Chair of Mechanical Engineering, Montanuniversität Leoben, 8700 Leoben, Austria; martin.leitner@unileoben.ac.at (M.L.); michael.stoschka@unileoben.ac.at (M.S.)

² Chair of Mechanical Engineering, Montanuniversität Leoben, 8700 Leoben, Austria; christian.garb@alumni.unileoben.ac.at (C.G.); florian.gruen@unileoben.ac.at (F.G.)

* Correspondence: roman.aigner@unileoben.ac.at; Tel.: +43-3842-402-1454

Received: 5 November 2018; Accepted: 4 December 2018; Published: 6 December 2018



Abstract: This paper contributes to the effect of elevated temperature on the fatigue strength of common aluminum cast alloys EN AC-46200 and EN AC-45500. The examination covers both static as well as cyclic fatigue investigations to study the damage mechanism of the as-cast and post-heat-treated alloys. The investigated fracture surfaces suggest a change in crack origin at elevated temperature of 150 °C. At room temperature, most fatigue tests reveal shrinkage-based micro pores as their crack initiation, whereas large slipping areas occur at elevated temperature. Finally, a modified $\sqrt{\text{area}}$ -based fatigue strength model for elevated temperatures is proposed. The original $\sqrt{\text{area}}$ model was developed by Murakami and uses the square root of the projected area of fatigue fracture-initiating defects to correlate with the fatigue strength at room temperature. The adopted concept reveals a proper fit for the fatigue assessment of cast Al-Si materials at elevated temperatures; in detail, the slope of the original model according to Murakami should be decreased at higher temperatures as the spatial extent of casting imperfections becomes less dominant at elevated temperatures. This goes along with the increased long crack threshold at higher operating temperature conditions.

Keywords: aluminum cast; fatigue strength; defects; hardness; tensile tests; elevated temperature

1. Introduction

Aluminum cast parts enable the manufacturing of quite complex geometries, due to their sound castability [1]. Furthermore, the investigated alloys also feature a proper fatigue strength; hence the achievement of lightweight design goals is additionally supported [2]. Therefore, Al-Si cast alloys are commonly used materials for automotive engine components, as reported in [3–6]. However, the manufacturing process, as well as the subsequent heat treatments, must be considered as they possess distinctive impacts on the resulting mechanical properties [7–9]. As such cast aluminum components are also exposed to elevated temperatures during service, the characterization of the material properties under these conditions is inevitable. Hence, the material properties of Al-Si cast alloys are investigated under elevated temperatures in a preliminary study [10]. This work extends the investigations from Garb et al. [10] by means of sampling positions, the statistical evaluation of fatigue fracture-initiating inhomogeneities and a defect-based fatigue strength model at elevated temperature of 150 °C, which was chosen in this study to reflect typical service conditions [11]. Another study [12] proposed the estimation of fatigue life under enhanced temperatures from tensile

test results. Yet, increased temperatures significantly influence the microstructure as well as the fatigue lifetime [13,14]. The corresponding investigated sampling position parts can inherit different local microstructures due to the varying local cooling conditions. Therefore, the inhomogeneities and their statistically distribution regarding shape and spatial extent differ from each sample position to another. Tiryakioğlu proposed in [15] that fatigue-initiating defect sizes in aluminum cast material can be properly described by Gumbel [16], see Equation (1) or the Generalized Extreme Value distribution [17], see Equation (2).

$$G_{(d_{eq})} = \exp \left[-\exp \left(-\frac{d_{eq} - \lambda}{\delta} \right) \right] \quad (1)$$

With $G_{(d_{eq})}$ being the cumulative distribution function of the Gumbel distribution, its course is characterized by the distribution parameters λ and δ , also referred to as location and scale parameter.

$$P_{(d_{eq})} = \exp \left\{ - \left[1 + \zeta \left(\frac{d_{eq} - \mu}{\sigma} \right)^{-\frac{1}{\zeta}} \right] \right\} \quad (2)$$

Furthermore, $P_{(d_{eq})}$ equals the cumulative distribution function of the Generalized Extreme Value distribution depending on the equivalent circle diameter d_{eq} , the location μ , the scale σ and the shape parameter ζ . Furthermore, it was shown that the fatigue strength in the finite life region can be assessed by linking the cumulative probability density of fracture-initiating defect size distribution with the Paris-Erdoğan equation for stable crack growth [18]. Due to the fact that the focus of this work is the fatigue strength assessment of Al-Si cast materials in the long-life fatigue region, Murakami's \sqrt{area} concept is used, see [19]. Hereby, the author in [19] stated that in the presence of extrinsic heterogeneities, such as flaws, the fatigue strength correlates well with the size of those defects. The spatial extent of the fatigue fracture-initiating defects is characterized by the square root of defect projection area \sqrt{area} , whereby the area is projected onto the plane perpendicular to the direction of maximum stress. A summary of this procedure is additionally given in [20]. The \sqrt{area} is used as the size parameter of fatigue fracture-initiating flaws, due to the sound correlation with the maximal stress intensity factor at the crack tip K_{max} , see [20]. Murakami's approach is based on the material and defect location dependent coefficient C_1 , the material constants C_2 and m , as well as on the Vickers hardness HV, see Equation (3).

$$\sigma_{f,1E7} = C_1 \cdot \frac{(HV + C_2)}{\sqrt{area}^{1/(2-m)}} \quad (3)$$

Murakami proposed the exponent m of the defect size to possess a constant value of 3, which revealed sound results for preliminary studies [21]. Furthermore, Murakami estimated the material and defect location coefficient C_1 as 1.43 for surface and 1.56 for subsurface cracks and the material dependent parameter C_2 to possess a constant value of 120 by applying the least squares method [19].

To assess the fatigue strength for operating conditions, this paper focuses on the influence of elevated temperature on the mechanical properties of two Al-Si cast materials, namely EN AC-46200 and EN AC-45500. Both tensile tests to assess the quasi-static properties as well as fatigue tests are performed at room and at elevated temperature to assess an advanced fatigue strength model based on the \sqrt{area} -approach by Murakami [19,20]. In summary, this paper scientifically contributes with the following working packages:

- Investigation of the fatigue strength of Al-Si cast materials at an elevated temperature of 150 °C
- Assessment of statistically defect distribution regarding spatial extent and shape
- Investigation of damage mechanisms at enhanced operating temperatures
- Evaluation of the material constants C_1 , C_2 and m of Murakami's \sqrt{area} concept for elevated temperatures

2. Materials and Methods

2.1. Materials

The examined materials are two Al-Si cast alloys with Strontium (Sr) as eutectic modifier and post-heat treatments to obtain T5 and T6 condition, see previously performed studies [10,22,23]. The T5 heat treatment consists of a quenching process and subsequent artificial aging whereas the T6 heat treatment usually involves three stages; the solution treatment at high temperatures, the quenching, and the age hardening process [24]. A summary of the T6 heat-treatment procedure and its impact on the resulting mechanical properties, depending on the chemical composition of the alloy and the exposure temperature and time, is given in [25]. The specimens are taken from gravity casted crankcases (CC) and cylinder-heads (CH) from varying positions (denoted as Pos #1 to Pos #3) exhibiting different local cooling conditions and therefore a variation in microstructure such as secondary dendrite arm spacing (sDAS) and micro pore size distribution. The nominal chemical composition of the investigated alloys is given in Table 1. The eutectic modifier Sr acts as micro alloying element and is measured in the ppm-range in the final cast material condition.

Table 1. Nominal chemical composition of the investigated cast alloys in weight percent.

Alloy	Si [%]	Cu [%]	Fe [%]	Mn [%]	Mg [%]	Ti [%]	Al [-]
EN AC-46200	7.5–8.5	2.0–3.5	0.8	0.15–0.65	0.05–0.55	0.25	balance
EN AC-45500	6.5–7.5	0.2–0.7	0.25	0.15	0.45	0.20	balance

In addition, an overview of the component's material specifications is listed in Table 2.

Table 2. Material specifications.

Part	Position	Alloy	Modifier	Heat Treatment	sDAS [μm]
CH	Pos #1	EN AC-46200	Sr	T5	24 ± 4.8
CC	Pos #2	EN AC-46200	Sr	T6	30 ± 7.3
CC	Pos #3	EN AC-46200	Sr	T6	72 ± 24.9
CH	Pos #1	EN AC-45500	Sr	T6	27 ± 6.6

2.2. sDAS and Metallographic Analysis

The sDAS is evaluated by means of a procedure proposed by [26], referred to as measurement method D. Hereby, metallographic specimens are taken out at the very sample positions and prepared by polishing. Afterwards, the specimens are investigated by digital optical microscopy. The secondary dendrite arm spacing is then calculated invoking the number of secondary arms along one side of a primary arm, such that dendrite asymmetry does not affect this method. This procedure is used, as it provides the most accurate estimation of secondary dendrite arm spacing, according to [26]. The investigation of metallographic sections in the testing region proposes a similar secondary dendrite arm spacing of Pos #1 for both alloys. The investigation of metallographic parameters in Pos #2 proposes a slightly enhanced local sDAS of 30 μm , regarding the values of Pos #1. The evaluated sDAS in sampling position Pos #3 is significantly higher though, due to lower cooling conditions compared to Pos #1 and #2, see [27]. The hardness measurements are conducted by means of a system of the type Zwick ZHU 2.5 TS1S (Ulm, Germany) and the metallographic samples are prepared by means of a Buehler BETA and a Struers CitPress system.

2.3. Quasi-Static and Fatigue Testing

The evaluation of the quasi-static material properties is carried out for room and elevated temperature, see [28] and [29] respectively. Each test series contains a minimum number of three specimens to statistically assess quasi-static properties. All tensile specimens and are conducted

strain-controlled at a strain rate of 3.6×10^{-3} 1/s with a gauge length of $l_0 = 25$ mm, using an extensometer. Both the tensile tests and the fatigue tests are conducted at a hydraulic Instron Schenk testing system. To additionally evaluate both the fatigue strength and yield strength of the investigated materials not only at room but also at the ET of 150 °C, an Instron SFL 3119-400 Series temperature controlled chamber (Darmstadt, Germany) is used. The tensile test specimen geometry is displayed in Figure 1.

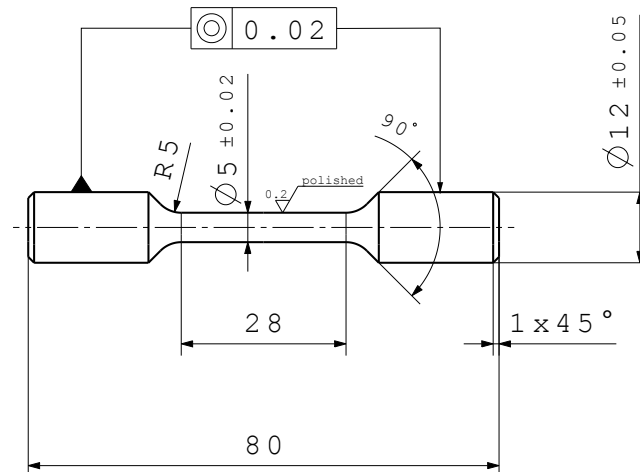


Figure 1. Tensile test specimen geometry in units of millimetre.

2.4. X-ray Computed Tomography

The investigated samples possess a low density and a small specimen diameter. Thus, the non-destructive investigation of selected specimens is carried out by a Phoenix/X-ray Nanotom 180, enabling a resolution of just 5 μm voxel-size, such that extrinsic flaws with a spatial extent of about 15 μm can be evaluated properly.

3. Results

3.1. Tensile Tests

Preliminary studies [30] stated that the fatigue resistance correlates linearly with the quasi-static material properties as the ultimate tensile strength (UTS) or the yield stress (YS) at corresponding temperatures. Furthermore, it is well known that exposure of Al-Si cast material at enhanced temperature leads to a significant decrease of the fatigue resistance [14]. Therefore, quasi-static tensile tests are not only conducted at room temperature, but also at an elevated temperature of 150 °C, using a heat chamber. An overview of the quasi-static test results is provided in Table 3.

Table 3. Results of quasi-static tensile tests.

Abbreviation	Temperature	UTS [MPa]	YS [MPa]	A [%]
EN AC-46200 Pos #2	RT	326	277	1.58
EN AC-46200 Pos #2	ET	265	245	2.96
EN AC-46200 Pos #3	RT	208	207	0.18
EN AC-46200 Pos #3	ET	187	187	0.19
EN AC-46200 Pos #1	RT	287	198	2.31
EN AC-46200 Pos #1	ET	234	184	5.25
EN AC-45500 Pos #1	RT	334	273	6.78
EN AC-45500 Pos #1	ET	259	233	9.55

EN AC-45500 Pos #1 reveals the highest UTS with 334 MPa at room temperature. In addition, EN AC-45500 Pos #1 also possesses the highest fracture elongation values A at room and elevated

temperature. As listed in Table 3, the fracture elongation increases if tested at elevated compared to room temperature.

The results confirm preliminary studies [31], which proposed a function of the ascending elongation with increasing testing temperature. Yet, the authors in [31] do not register a significant increase of A below 270 °C. Another study [32] shows a strong increase of the elongation at fracture only for testing temperatures above 300 °C testing temperature. However, the test results observed in this study propose an increased fracture elongation already at 150 °C for the examined alloys, see Figure 2. Figure 2 displays representative tensile test results for the varying sampling positions at room and elevated temperature. Furthermore, representative microstructures at the very specimen locations are illustrated in detail in Figure 3.

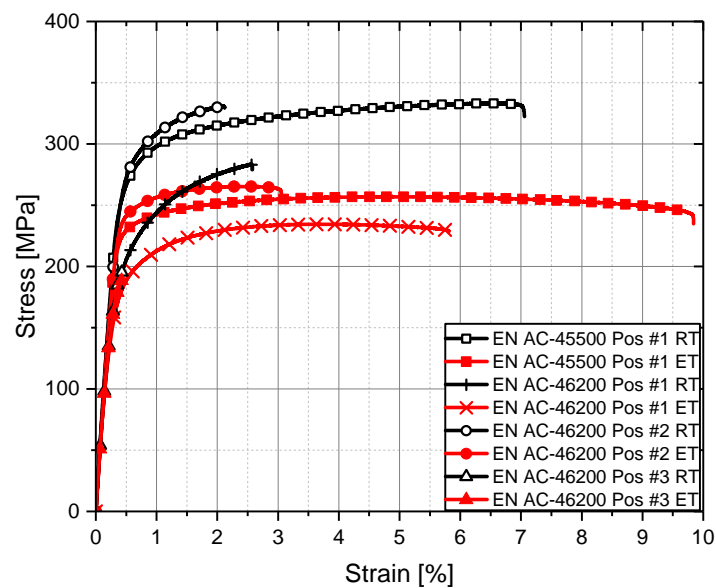


Figure 2. Representative tensile test curves at RT and ET.

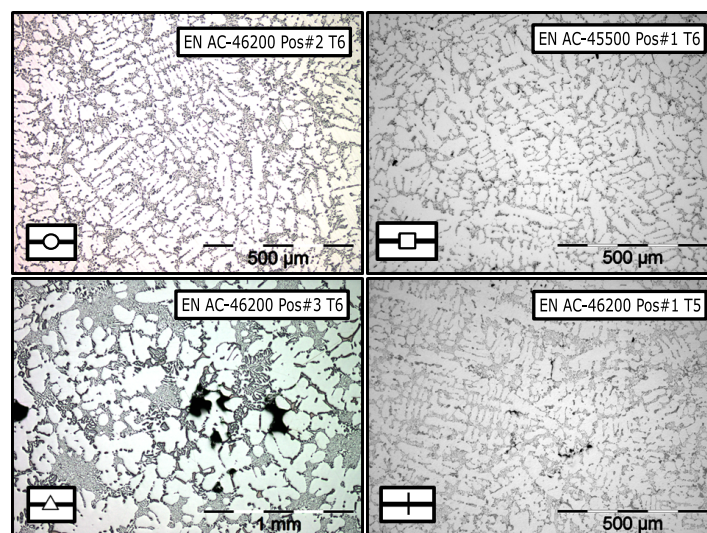


Figure 3. Microstructure at the investigated sample positions.

On the other hand, the yield strength in general decreases at elevated temperature, as listed in Table 3. The mean reduction of the UTS from room to elevated temperature is approximately 17%. This goes along with preliminary studies in [31–33].

3.2. Hardness Measurements

As stated in [34,35] the quasi-static material properties such as the yield strength exhibit a basic coherence with the macrohardness. Also, the investigation of the position depending hardness is from significance to set up Murakami's $\sqrt{\text{area}}$ model [19] in a uniform way for the investigated specimen series. Therefore, Vickers hardness measurements are executed at room temperature in line with [36] applying a testing force of 3 kp. A preliminary study [37] describes a linear relationship of Al-Zn-Mg alloys between the Vickers hardness HV and the flow stress. In [38] it is also stated that the Brinell hardness BHN corresponds well to the YS for both A356 and A357 alloys. In [39] an evaluation of models for hardness-yield strength relationships is presented. Drouzy and Richard [40] presented a quite simple linear ratio between the YS and the Brinell hardness BHN of underaged Al-Si alloys. However, it is also shown that the YS-BHN relationship of Al-Si alloys can be rather described by a hysteresis, which shows a significantly higher slope in the underaged region than the proposed relationship from [40]. Murakami's $\sqrt{\text{area}}$ model takes the local Vickers hardness HV into account, as it relates well to the fatigue strength [20]. Therefore, the local hardness for the sample positions must be investigated not only at room but also at elevated temperatures.

To estimate the hardness at an elevated temperature, a linear fit, using the least square method, between the measured hardness and calculated yield strength, is carried out, see Figure 4. The evaluated slope of the fit is almost two times the proposed value of approximately 2.85 from [40]. Each test series contains a minimum number of three tensile specimens and three hardness tests at the corresponding position to tone down outlier values. Subsequently, the yield strength of tensile tests at elevated temperatures is re-inserted in the estimated YS-HV fit, to estimate the Vickers hardness at elevated temperatures.

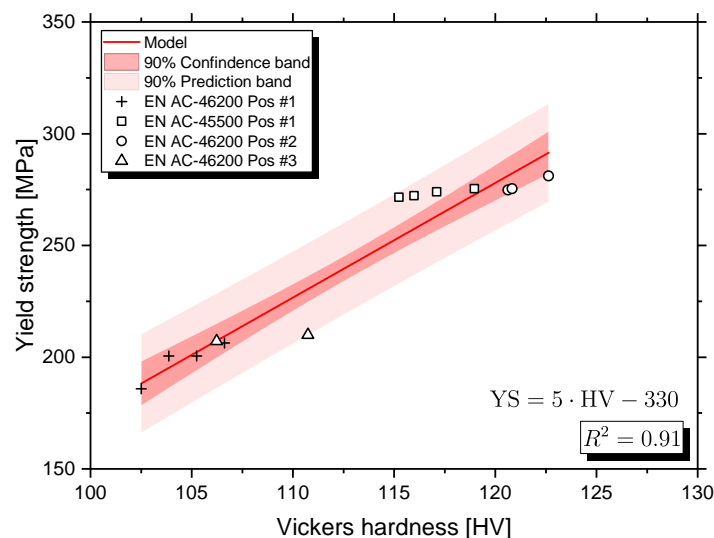


Figure 4. Evaluated correlation between Vickers hardness and Yield strength for Al-Si castings.

3.3. Fatigue Tests

The fatigue tests are conducted under alternating tension-compression testing. This deduces a load stress ratio, lower load level to upper load level, of $R = -1$. Therefore, the mean stress is equal to zero. All fatigue tests are executed at a hydraulic testing machine with a testing frequency of 30 Hz until either specimen burst failure or run out at 1×10^7 load cycles. In line with the quasi-static tests, the fatigue tests at elevated temperature are performed using a heat chamber. The fatigue resistance in the finite life region is statistically evaluated by means of the ASTM E 739 standard [41]. This methodology assumes a constant variance in the finite life region. Furthermore, the fatigue data in the run out region is statistically investigated based on the $\arcsin \sqrt{p}$ methodology, see [42]. This procedure approximates the probabilities of survival in the long-life region by a $\arcsin \sqrt{p}$ function

and is a proven methodology to statistically estimate the mean value and standard deviation of the fatigue strength and likewise minimum life, see [43]. As proposed in [44], the slope k_2 of the run out region is assumed to be five times the slope k_1 in the finite life region. This assumption is also verified in [45–47]. All fatigue data has been normalized by the UTS at room temperature of EN AC-46200 -Pos #2, evaluated to 326 MPa, see Table 3.

The tests are performed until a total number of 1×10^7 load cycles, because preliminary studies showed defect correlated specimen failure in the HCF region between 1×10^6 and 1×10^7 load cycles, see [3,48,49]. All evaluated S/N-curves are displayed including the 10 and 90 % probability of survival scatter band. The statistical evaluation of scatter bands in the run out region is conducted by means of the $\arcsin \sqrt{p}$ methodology [42,43]. The evaluated fatigue strength data for each sample position as well as the scatter band in the run out region is listed in Table 4. In Figure 5 the S/N-curve of EN AC-45500 with T6 heat treatment at Pos #1 at room and at elevated temperature is displayed. While the slope k_1 is almost identical for RT and ET, the number of cycles N_D for the transition region rises with increased testing temperature from approximately 1×10^6 to about 4.27×10^6 load cycles. The investigated fatigue strength of EN AC-46200 with T5 heat treatment at Pos #1 states also a similar k_1 at room temperature, see Figure 6. On the other hand, the high-cycle fatigue strength at 1×10^7 load cycles $\sigma_{f,1 \times 10^7}$ significantly decreases by about 21 % at 150 °C. The investigation of the fatigue strength from EN AC-46200 with T6 heat treatment at Pos #2 assumes a slightly shallower S/N-curve at elevated temperature, represented by the slope in the finite life region k_1 . Furthermore, the transition point N_D rises to 1.75×10^6 load cycles, with a decrease of about 7% in fatigue strength $\sigma_{f,1 \times 10^7}$, as seen in Figure 7. Finally, EN AC-46200 with T6 heat treatment at Pos #3 shows a significant shallower slope in the finite life region k_1 , while the evaluated fatigue resistance $\sigma_{f,1E7}$ decreases only by 2% at 150 °C testing temperature, see Figure 8. It must be pointed out that the depicted minor reduction of the fatigue strength in Pos #3 is within the scatter band of the S/N-curves.

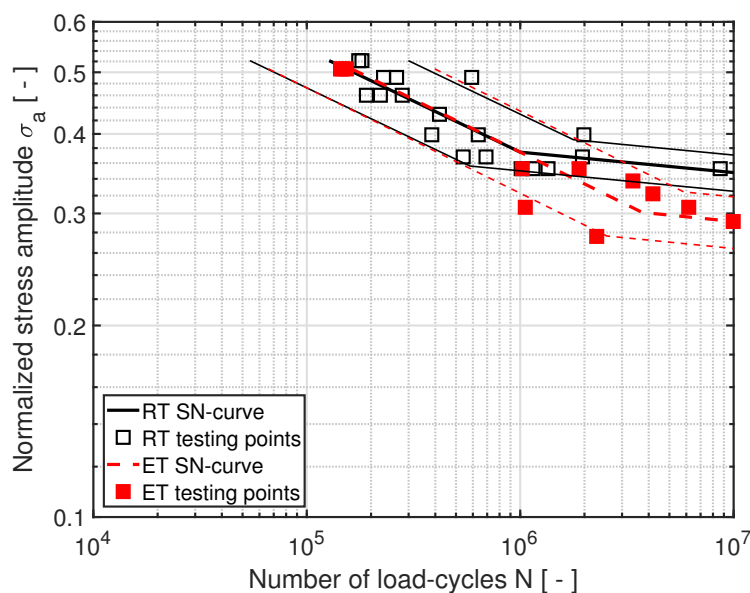


Figure 5. S/N-curves of EN AC-45500 T6 Pos #1 at RT and ET.

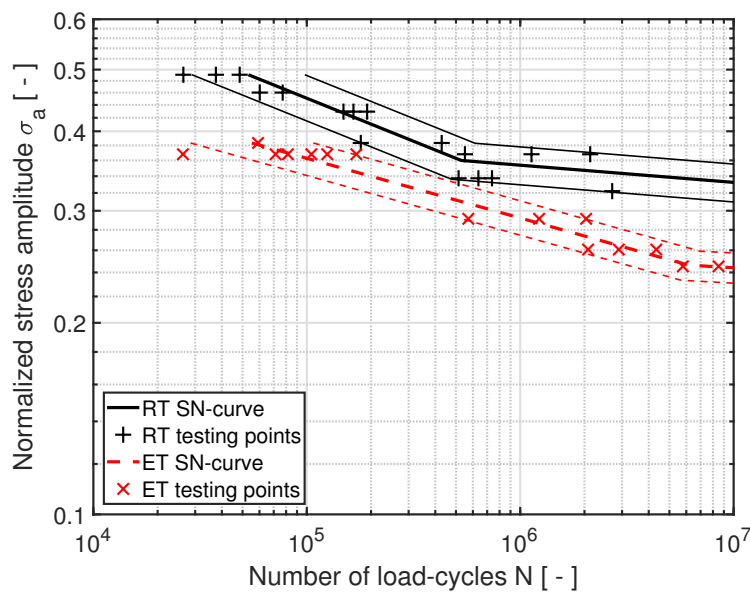


Figure 6. S/N-curves of EN AC-46200 T5 Pos #1 at RT and ET.

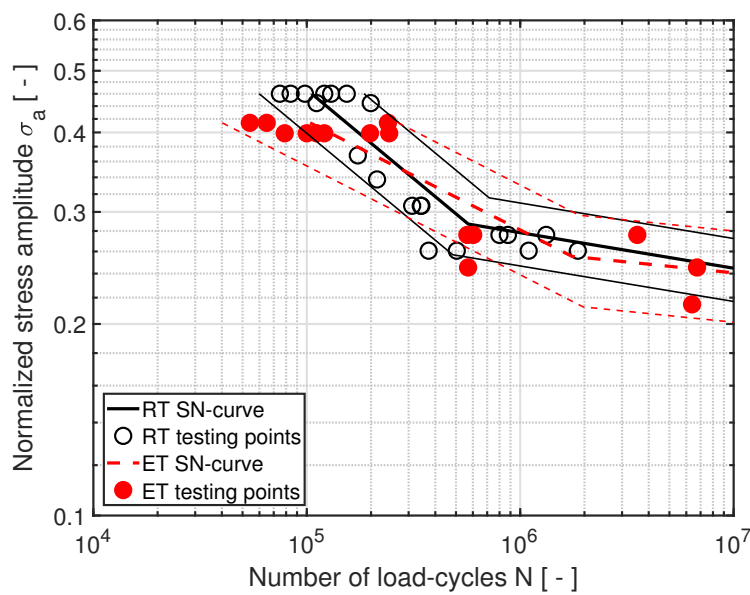


Figure 7. S/N-curves of EN AC-46200 T5 Pos #2 at RT and ET.

Table 4. Fatigue test results at room and elevated temperature.

Abbreviation	Temperature	$\sigma_{1 \times 10^7, norm}$	N_D	k_1	$\frac{1}{T_s}$
EN AC-46200 Pos#2	RT	0.245	5.71×10^5	3.58	1.256
EN AC-46200 Pos#2	ET	0.241	1.75×10^6	5.85	1.391
EN AC-46200 Pos#3	RT	0.176	3.92×10^6	5.13	1.278
EN AC-46200 Pos#3	ET	0.172	2.68×10^6	6.41	1.210
EN AC-46200 Pos#1	RT	0.332	5.29×10^5	7.40	1.147
EN AC-46200 Pos#1	ET	0.244	6.16×10^6	10.65	1.115
EN AC-45500 Pos#1	RT	0.348	9.99×10^5	6.22	1.140
EN AC-45500 Pos#1	ET	0.291	4.27×10^6	7.48	1.206

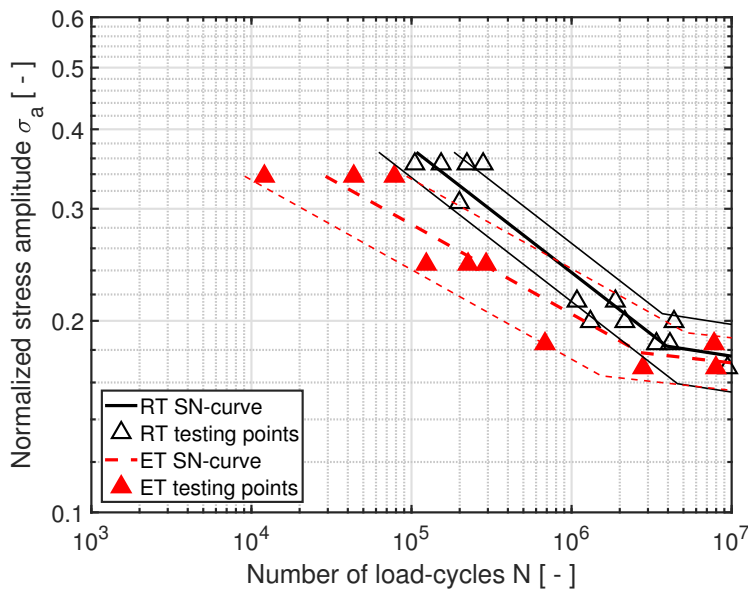


Figure 8. S/N-curves of EN AC-46200 T5 Pos #3 at RT and ET.

To investigate the fracture-initiating defects, it is from utmost importance to analyze all tested specimens either by means of digital microscope as well as by SEM. The detected crack-initiating flaws are characterized by means of geometrical parameters such as the square root of the effective defect area. In line with the procedure proposed in [20], the size of fatigue fracture-initiating defects is characterized by the square root of the projected area of the flaw, perpendicular to the load direction. This methodology is displayed in Figure 9 using the example of a fracture-initiating heterogeneity at Pos #3. Furthermore, to characterize not only the fracture-initiating defects by means of fractography, selected specimens are investigated non-destructively with X-ray computed tomography (XCT). This methodology supports the holistic characterization of the defect population respectively its spatial extent and is further described in [22,48].

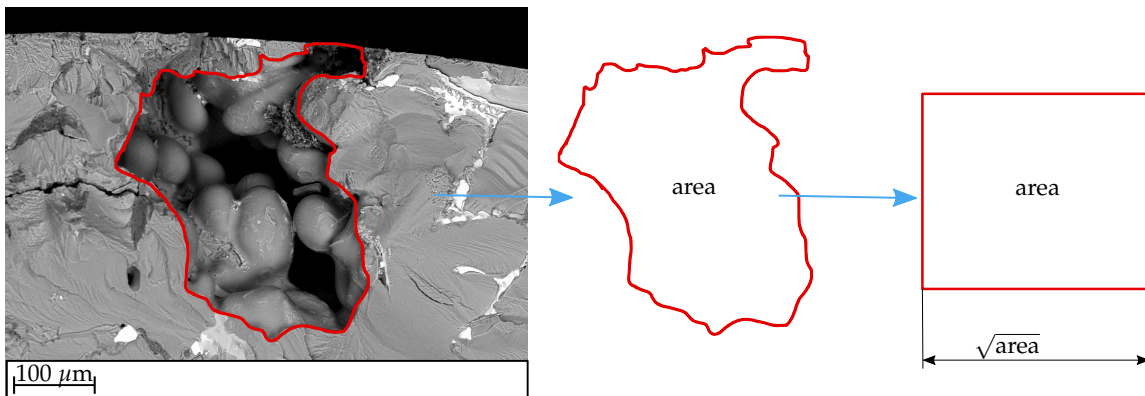


Figure 9. Defect size measurement methodology and representative fracture-initiating micropore at Pos#3.

Figures 9 and 10 show a fracture surface with a crack origin at a micro pore. At room temperature, all tested EN AC-46200 specimens initiate from a such micro pores. On the other hand, Figure 11 displays a different cause of failure. At ET, the stress intensity is enhanced in the defect-near area while the activation energy of slip-planes decreases due to the increased operating temperature. Therefore, specimens tested at a higher temperature activate a different failure mechanism.

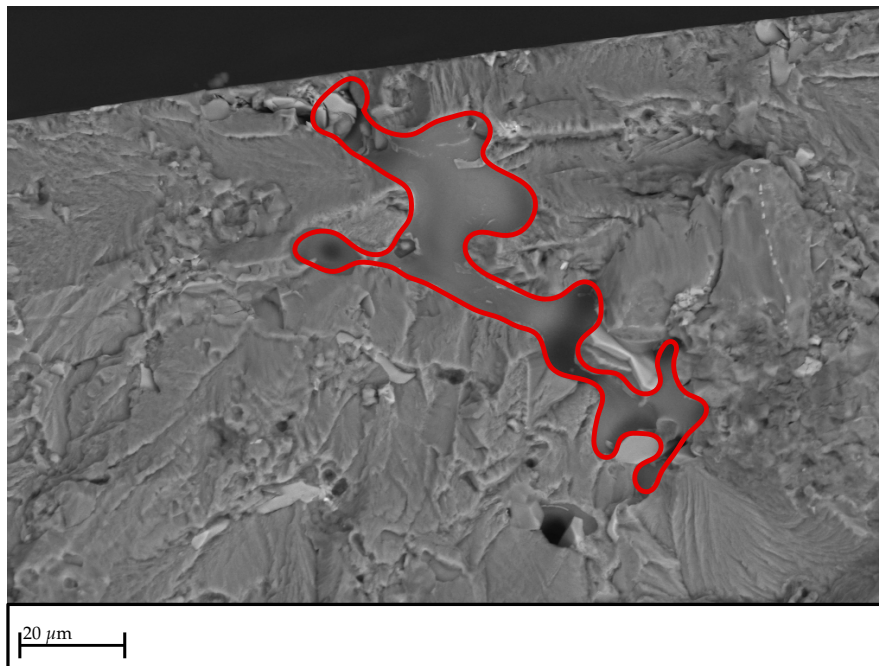


Figure 10. Representative fracture-initiating micropore at Pos#2.

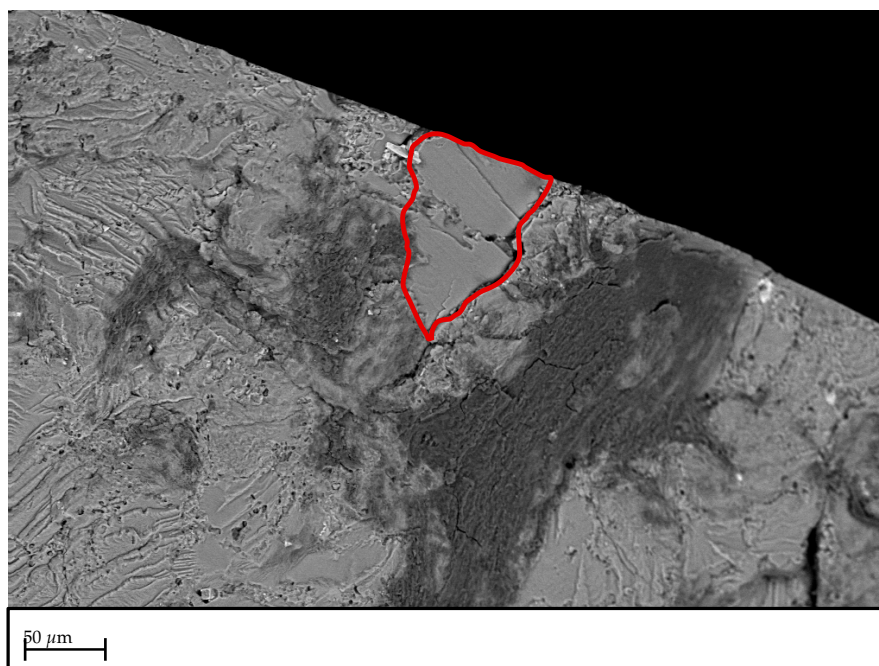


Figure 11. Representative fracture-initiating slipplane at Pos#1.

Some specimens would reveal a crack initiation right at the surface along with crack propagation at large slip bands. Nevertheless, some investigated specimens revealed mixed defect mechanisms of micro pores and large slipping areas. At the latter ones, the crack initiates at an intrinsic inhomogeneity and possesses a stable crack growth as with increasing crack length, the stress intensity rises near the crack tip. If the stress intensity factor and the activation energy based on the thermal energy reach a certain threshold, the crack starts to slip over a slip-band area during one single load-cycle and therefore significantly increases the crack growth. As a result, the remaining fatigue strength is reduced compared to an arbitrary defect with a similar $\sqrt{\text{area}}$.

As the fractography results show, this failure mechanism occurs especially at EN AC-46200 T5 and EN AC-45500 T6, where a major part of the specimens at Pos #1 inherit a slip-band-induced failure. It must be noted that EN AC-45500 T6 Pos #1 even shows a slip-band-like failure mechanism also at room temperature. In Figure 12, the different damage mechanism fractions of the corresponding positions and alloys are displayed.

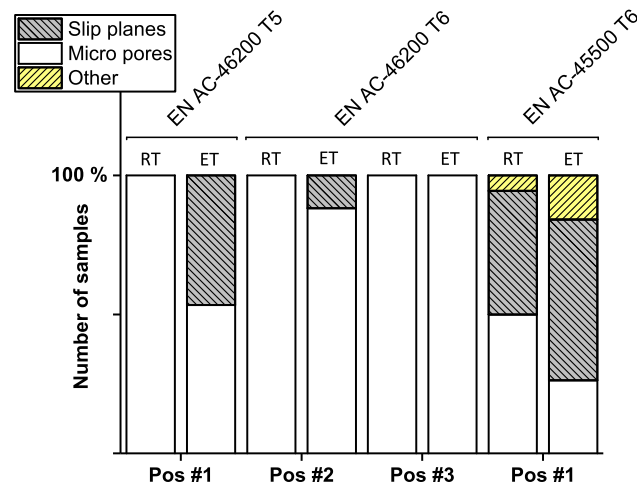


Figure 12. Comparison of the crack-initiating failures at RT and ET.

As proposed by [50] either Gumbel or GEV distributions are applicable for fatigue-initiating defects. The distribution parameters are evaluated by means of a maximum likelihood method, as presented in [51].

$$\phi = \frac{1}{n} \sum_{i=1}^n \frac{d_{eq,i}}{d_{max,i}} \quad (4)$$

The probability of occurrence of an arbitrary d_{eq} , based on the cumulative density function of the GEV-fit for each sampling position is displayed in Figure 13. The probability of occurrence of a d_{eq} of 200 μm is less than 10% for sampling positions #1 and #2, whereas at Pos #3 the probability of occurrence for the same equivalent diameter possesses a value of just above 97%.

The cumulative density function of the distribution is computed by means of Equation 2, using the equivalent circle diameter (d_{eq}) from the most critical defects, whereas ζ is denoted as the shape σ the scale and μ the location parameter. The equivalent circle diameter d_{eq} of one flaw can easily be derived by multiplying $\sqrt{\text{area}}$ with the factor $\frac{2}{\sqrt{\pi}}$. The ratio of the equivalent circle diameter d_{eq} to the maximum diameter d_{max} describes the shape ϕ of the crack-initiating pores [52], see Equation (4). The shape factor ϕ therefore ranges between zero and one, indicating the roundness of a crack-initiating pore. The lower ϕ , the more complexly shaped is the defect. Thus, a circle-shaped flaw would possess a shape factor $\phi = 1$. The shape of representative defects with varying sphericity is presented in detail in [53].

Both the evaluated distribution parameters as well as the mean shape of the defects are listed in Table 5. The investigation of the different fracture-initiating defect sizes proposes a significant different micro pore size distribution at Pos #3, in line with the increased local sDAS. The mean shape ϕ of the flaws in Pos #3 also reckon them to possess a more spherical shape.

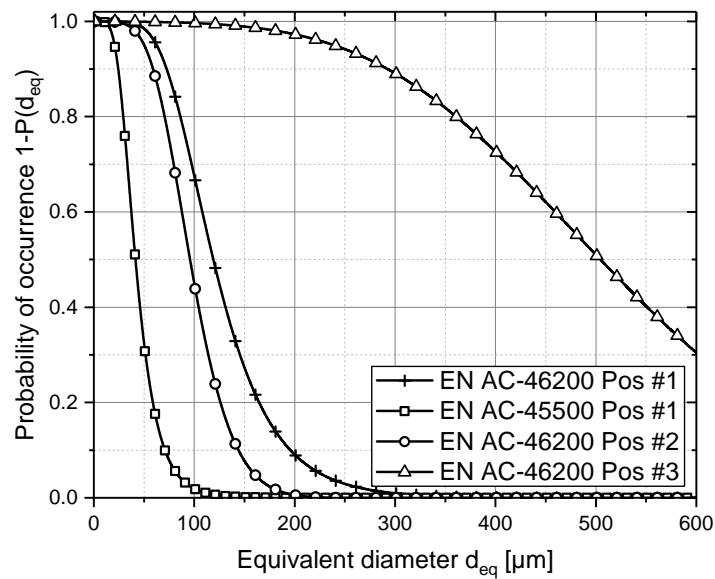


Figure 13. Probability of occurrence of fracture-initiating defects.

Table 5. GEV-fit parameters based on evaluated d_{eq} of fracture-initiating defects.

Abbreviation	ζ	σ	μ	ϕ
EN AC-46200 Pos #1	0.03	39.03	104.60	0.52
EN AC-46200 Pos #2	−0.12	29.83	85.10	0.48
EN AC-46200 Pos #3	−0.19	168.57	444.88	0.60
EN AC-45500 Pos #1	0.06	14.50	36.08	0.49

3.4. Fatigue Assessment Model

To assess the fatigue strength of Al-Si alloys incorporating manufacturing process-based inhomogeneities, a defect size-based material model is set up. The main causes of failure, evaluated in both EN AC-46200 Pos #1 and EN AC-45500 Pos #1, are basically not based on micro pores. Therefore, the defect-based material model from Murakami [19] is mainly set up for EN AC-46200 Pos #2 and Pos #3 as herein the main failure cause can be assigned to micro porosity. However, specimens with defect correlated crack initiation from Pos #1 of both alloys are also displayed in the adopted material model, see Figure 14. A parameter set, containing the stress amplitude at 1×10^7 load cycles $\sigma_{f,1 \times 10^7}$ of run-outs, the stress amplitude σ_a and number of load cycles N of tests in the finite life region, as well as the corresponding defect size \sqrt{area} are required. To increase the applicable data a power-function like projection method for specimens failed in the finite life region is executed. This method is suitable to increase the data points in the run out region of $N = 1 \times 10^7$ without significant falsification of the scatter band in the HCF region $1/T_s$, see [21].

The original data from Murakami [19] proposes a coefficient of $m = 3$ for the exponent of the defect size. The parameters C_1 and C_2 are material dependent constants. This approach provides reasonable defect-based material models for Al-Si alloys at room temperature. However, the exponent of the defect size can vary at elevated temperatures, as it represents the slope of the material model. Therefore, the coefficient m is not further considered to be a constant, see Equation (5).

$$\sigma_{1E7} = C_{1,T} \cdot \frac{(HV + C_{2,T})}{\sqrt{area}^{1/(2 \cdot m_T)}} \quad (5)$$

This model is supplied with all parameter sets depending on their alloy, position, and testing temperature. Furthermore, the hardness of the corresponding positions at elevated temperature is estimated based on the experimentally evaluated yield strength, as discussed in Section 3.2. Next, the parameters $C_{1,T}$ and $C_{2,T}$ as well as the slope m_T are estimated applying a non-linear

solver, using the least square method. The evaluated parameters maintain a slope of $m_T = 3.02$ for specimens tested at room temperature, which agrees with the proposed constant of $m = 3$ in the original model, see Equation (3). However, the data at elevated temperature leads to a change of the slope value. The least square method proposes a coefficient of $m_T = 4.05$ for specimens tested at an elevated temperature of 150 °C. The defect-based material model for elevated temperatures with the 90 and 10% probability scatter bands is displayed in Figure 14. The defect correlated fatigue strength is restricted by two major limits. On the one hand, the upper boundary is set by the fatigue strength of near defect-free material where the area of the crack-initiating inhomogeneities tends to zero. On the other hand, the lower boundary is determined by huge defects, such that the stress intensity factor along the internal crack meets the long crack threshold $\Delta K_{th,lc}$, see Equation (6).

$$\Delta K_{th,lc} = Y\Delta\sigma_{1E7}\sqrt{\pi\sqrt{area}} \quad (6)$$

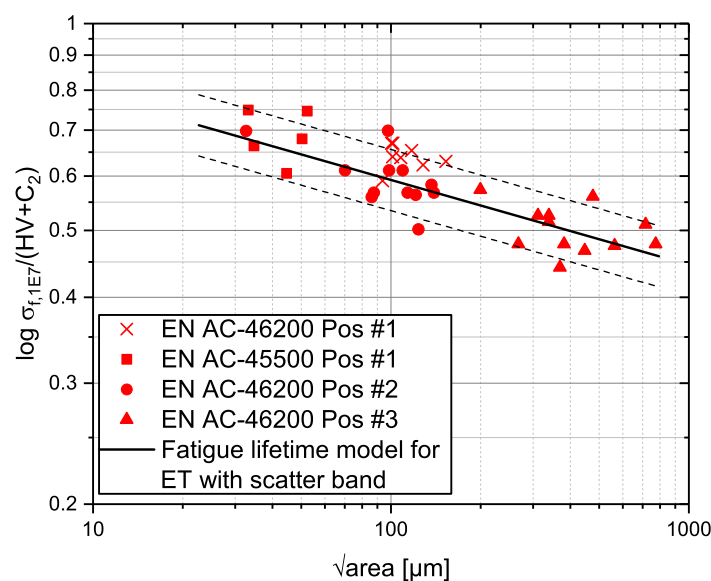


Figure 14. Defect correlated fatigue lifetime model with evaluated coefficient m at elevated temperature.

Preliminary studies [54–56] revealed that $\Delta K_{th,lc}$ rises in line with increasing testing temperature, until a critical temperature is met. This results from an increased plastic zone in front of the crack tip. The size of the monotonic plastic zone can be estimated by Irwin's estimation, based on the YS of the material, see Equation (7) [57].

$$r_{pl} = \frac{K^2}{\pi YS^2} \quad (7)$$

The relationship proposed by Irwin applies for a monotonic plastic zone with no crack closure occurring [58]. To evaluate the cyclic plastic zone, incorporating crack closure effects, K is superimposed by ΔK_{eff} , such that:

$$\Delta r_{pl} = \frac{\Delta K_{eff}^2}{\pi 4 YS^2} \quad (8)$$

As the YS decreases with elevated testing temperature at an average of 10.7%, the size of the cyclic plastic zone Δr_{pl} therefore rises by 25.4%, see Equation (8). Hence, the plastic-induced crack closure effects significantly increase, in line with the extended plastic zone [59–61], resulting in an elevated long crack threshold $\Delta K_{th,lc}$ at higher temperatures. As a result, defects with large spatial extent do not affect the fatigue strength at elevated temperatures as significantly as for room temperatures,

see Equation (6). The increased slope of the defect-based material model, represented by the coefficient m_T , thus is deduced by increased $\Delta K_{th,lc}$ at elevated temperatures.

4. Discussion

In this paper, fatigue strength, hardness and quasi-static tests are executed at both RT and an ET of 150 °C. The investigated materials are different Al-Si alloys with subsequent T5 or T6 heat treatment and varying local solidification times, leading to locally adjusted microstructural features, such as secondary dendrite arm spacing and micropore distribution. Furthermore, fractographic analysis is conducted to evaluate the fracture-initiating defects and their spatial extent. To consider the decreasing hardness at elevated temperature, a linear relation between the yield strength and Vickers hardness is evaluated to establish a link between room- and elevated temperature data. The hardness at elevated temperatures is subsequently estimated based on quasi-static test results at 150 °C testing temperature, using the evaluated YS-HV relationship displayed in Figure 4. The investigation of the fatigue strength at elevated temperature reveals a significant decrease of 21% for specimen Pos #1 of both observed alloys in respect to the fatigue strength at room temperature. The evaluation of fatigue strength at elevated temperature at specimen Pos #2 and Pos #3 revealed a minor decrease of 2%, though. The tensile test data at elevated temperature reveals an overall increase of elongation at fracture of about 65%, as well as a decrease of Young's modulus of about 4%, due to elevated dislocation mobility. The specimen positions inherit major differences in fatigue fracture-initiating defects, as the statistical evaluation of flaw sizes states. This is mainly caused by the local significantly varying cooling rates between the sample positions and results in a broad spectrum of fatigue fracture-initiating material heterogeneities. Hence, the commonly used \sqrt{area} fatigue strength assessment model proposed by Murakami can be invoked as basic fatigue assessment strategy. The extended model, introduced in this paper, takes a modified and temperature dependent slope value of $m_T \approx 4$ into account to properly assess the fatigue strength in the long-life region at elevated temperatures, see Equation (5).

As shown in Figure 15, the proposed fatigue assessment model is compared with the normalized experimental results. The model for elevated temperatures properly meets the experimental fatigue lifetime data. The scatter band and the mean value are statistically estimated, approaching the methodology from [41]. The statistically evaluation of the fatigue assessment model reveals a comparably minor scatter band $1/T_m$ of 1.18.

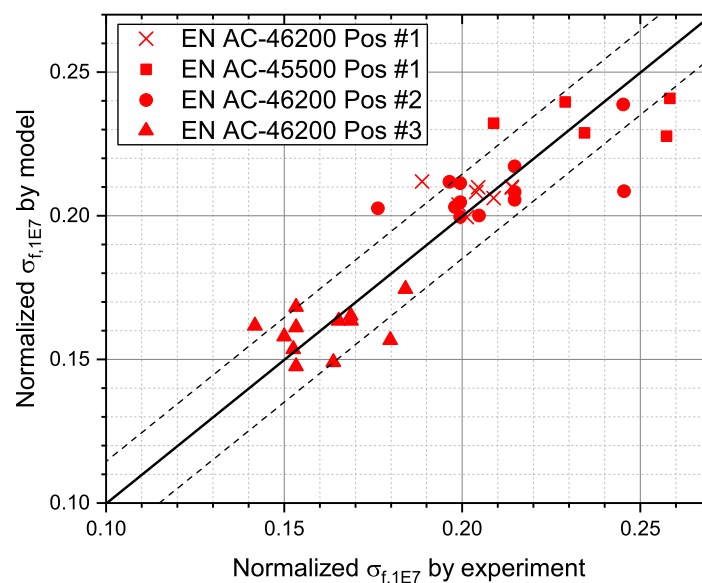


Figure 15. Validation of the \sqrt{area} model for elevated temperatures.

5. Conclusions

Based on the conducted research work and assessed results, the following conclusions can be drawn:

- The statistically evaluated fatigue strength of all tested alloys drops when being exposed at elevated temperatures compared to fatigue lifetime at room temperature.
- A significant change in damage mechanism at elevated temperatures is observed. A major part of the specimens taken from both EN AC-46200 Pos #1, as well as EN AC-45500 Pos #1, maintain slipping areas as crack origins.
- While the original \sqrt{area} model proposed by Murakami provides a sound fit for room temperature with a slope of $m = 3$, the slope changes at elevated temperature. The estimated slope $m_T \approx 4$ suggests an increased long crack threshold at elevated temperature, caused by more pronounced plasticity-induced crack closure effects. Therefore, the impact of increasing defect sizes on the anticipated fatigue resistance generally declines at elevated temperatures.
- Comparing the fatigue strength of the introduced extension of Murakami's model for higher operating temperatures, the experiments reveal a proper relationship. The mean value of the suggested model turns out to be slightly conservative.

Subsequent work focuses on the validation of the proposed model for further elevated temperature values incorporating additional fatigue tests. Moreover, the yield strength versus hardness relationship may be investigated in more detail at higher temperatures by additional testing series. Finally, near defect-free material must be experimentally analyzed in terms of fatigue strength at elevated temperatures to define the very upper boundary of the defect-based material model most accurately.

Author Contributions: Conceptualization, R.A., C.G. and M.L.; methodology, R.A., C.G. and M.L.; software, R.A. and C.G.; validation, R.A. and M.L.; formal analysis, R.A. and M.L.; investigation, R.A. and C.G.; resources, M.S. and F.G.; data curation, R.A. and C.G.; writing—original draft preparation, R.A.; writing—review and editing, M.L. and M.S.; visualization, R.A.; supervision, M.S. and M.L.; project administration, M.S. and F.G.; funding acquisition, M.S. and F.G.

Acknowledgments: The financial support by the Austrian Federal Ministry for Digital and Economic Affairs and the National Foundation for Research, Technology and Development is gratefully acknowledged. Furthermore, I would like to thank the industrial partners BMW München Group and Nematik Dillingen GmbH for the excellent mutual scientific cooperation within the CD-laboratory framework. The authors would like to thank Nematik Linz and Nematik Dillingen for providing the cast components. Further on, execution of the CT scans at the Materials Center Leoben GmbH is highly appreciated. Finally, financial project support was gladly provided by MAGMA Gießereitechnologie GmbH and AVL List GmbH. Financial support by the Austrian Federal Government (in particular from Bundesministerium für Verkehr, Innovation und Technologie and Bundesministerium für Wissenschaft, Forschung und Wirtschaft) represented by Österreichische Forschungsförderungsgesellschaft mbH and the Styrian and the Tyrolean Provincial Government, represented by Steirische Wirtschaftsförderungsgesellschaft mbH and Standortagentur Tirol, within the framework of the COMET Funding Programme is gratefully acknowledged.

Conflicts of Interest: The authors declare no conflict of interest. The founding sponsors had no role in the design of the study; in the collection, analyses, or interpretation of data; in the writing of the manuscript, or in the decision to publish the results.

Abbreviations

The following abbreviations are used in this manuscript:

RT	Room temperature
ET	Elevated temperature
λ	Location parameter of the Gumbel distribution
δ	Scale parameter of the Gumbel distribution
GEV	Generalized Extreme Value distribution
ξ, σ, μ	Shape, scale, and location parameter of the GEV

$\sigma_{f,1 \times 10^7}$	Long-life fatigue strength amplitude at 1×10^7 load cycles
$\Delta\sigma_{1 \times 10^7}$	Long-life fatigue strength range at 1×10^7 load cycles
σ_a	Fatigue strength amplitude
HV	Vickers hardness
$C_1, C_{2,m}$	Constants of the \sqrt{area} approach by Murakami
sDAS	Secondary dendrite arm spacing
YS	Yield strength
UTS	Ultimate tensile strength
HCF	High-cycle fatigue
E	Young's modulus
A	Fracture elongation
N_D	Number of load cycles at transition knee point of S/N-curve
N	Number of load cycles until failure
k_1	Slope in the finite life region of S/N-curve
T_S	Scatter band of S/N-curve in the HCF region
BHN	Brinell hardness number
SEM	Scanning-electron-microscopy
XCT	X-ray computed tomography
d_{eq}	Equivalent circle diameter
d_{max}	Maximal spatial extent of an inhomogeneity
ϕ	Shape factor
n	Number of defects
$C_{1,T}, C_{2,T}, m_T$	Parameters of the extended \sqrt{area} approach for elevated temperatures
K	Stress intensity factor
K_{max}	Maximal stress intensity factor
$\Delta K_{th,lc}$	Long crack threshold
ΔK_{eff}	Effective crack threshold
Y	Geometry factor
Δr_{pl}	Cyclic plastic zone
r_{pl}	Monotonic plastic zone
T_m	Scatter band of the validation of the fatigue assessment model

References

- Di Sabatino, M.; Arnberg, L. Castability of aluminium alloys. *Trans. Indian Inst. Met.* **2009**, *62*, 321–325. [[CrossRef](#)]
- Canales, A.A.; Carrera, E.; Silva, J.T.; Valtierra, S.; Colás, R. Mechanical properties in as-cast and heat treated Al-Si-Cu alloys. *Int. J. Microstruct. Mater. Prop.* **2012**, *7*, 281. [[CrossRef](#)]
- González, R.; González, A.; Talamantes-Silva, J.; Valtierra, S.; Mercado-Solís, R.D.; Garza-Montes-de Oca, N.F.; Colás, R. Fatigue of an aluminium cast alloy used in the manufacture of automotive engine blocks. *Int. J. Fatigue* **2013**, *54*, 118–126. [[CrossRef](#)]
- Mattos, J.; Uehara, A.Y.; Sato, M.; Ferreira, I. Fatigue properties and micromechanism of fracture of an AlSiMg0.6 cast alloy used in diesel engine cylinder head. *Procedia Eng.* **2010**, *2*, 759–765. [[CrossRef](#)]
- Mbuya, T.O.; Sinclair, I.; Moffat, A.J.; Reed, P. Micromechanisms of fatigue crack growth in cast aluminium piston alloys. *Int. J. Fatigue* **2012**, *42*, 227–237. [[CrossRef](#)]
- Javidani, M.; Larouche, D. Application of cast Al-Si alloys in internal combustion engine components. *Int. Mater. Rev.* **2014**, *59*, 132–158. [[CrossRef](#)]
- Tabibian, S.; Charkaluk, E.; Constantinescu, A.; Guillemot, G.; Szymtka, F. Influence of process-induced microstructure on hardness of two Al-Si alloys. *Mater. Sci. Eng. A* **2015**, *646*, 190–200. [[CrossRef](#)]
- Lu, L.; Nogita, K.; Dahle, A.K. Combining Sr and Na additions in hypoeutectic Al-Si foundry alloys. *Mater. Sci. Eng. A* **2005**, *399*, 244–253. [[CrossRef](#)]
- Yang, H.; Ji, S.; Fan, Z. Effect of heat treatment and Fe content on the microstructure and mechanical properties of die-cast Al-Si-Cu alloys. *Mater. Des.* **2015**, *85*, 823–832. [[CrossRef](#)]

10. Garb, C.; Leitner, M.; Grün, F. Effect of elevated temperature on the fatigue strength of casted AlSi8Cu3 aluminium alloys. *Procedia Struct. Integr.* **2017**, *7*, 497–504. [[CrossRef](#)]
11. Molina, R.; Amalberto, P.; Rosso, M. Mechanical characterization of aluminium alloys for high temperature applications Part1: Al-Si-Cu alloys. *Metall. Sci. Technol.* **2011**, *29*, 5–15.
12. Özdeş, H.; Tiryakioğlu, M. On estimating high-cycle fatigue life of cast Al-Si-Mg-(Cu) alloys from tensile test results. *Mater. Sci. Eng. A* **2017**, *688*, 9–15. [[CrossRef](#)]
13. Ceschini, L.; Morri, A.; Toschi, S.; Seifeddine, S. Room and high temperature fatigue behaviour of the A354 and C355 (Al-Si-Cu-Mg) alloys: Role of microstructure and heat treatment. *Mater. Sci. Eng. A* **2016**, *653*, 129–138. [[CrossRef](#)]
14. Konečná, R.; Nicoletto, G.; Kunz, L.; Riva, E. The role of elevated temperature exposure on structural evolution and fatigue strength of eutectic AlSi12 alloys. *Int. J. Fatigue* **2016**, *83*, 24–35. [[CrossRef](#)]
15. Tiryakioğlu, M. Statistical distributions for the size of fatigue-initiating defects in Al-7%Si-0.3%Mg alloy castings: A comparative study. *Mater. Sci. Eng. A* **2008**, *497*, 119–125. [[CrossRef](#)]
16. Gumbel, E.J. *Statistics of Extremes*; Columbia University Press: New York, NY, USA, 1958.
17. Jenkinson, A.F. The frequency distribution of the annual maximum (or minimum) values of meteorological elements. *Q. J. R. Meteorol. Soc.* **1955**, *87*, 145–158. [[CrossRef](#)]
18. Tiryakioğlu, M. Relationship between Defect Size and Fatigue Life Distributions in Al-7 Pct Si-Mg Alloy Castings. *Metall. Mater. Trans. A* **2009**, *40*, 1623–1630. [[CrossRef](#)]
19. Murakami, Y. *Metal Fatigue: Effects of Small Defects and Nonmetallic Inclusions*; Elsevier: Amsterdam, The Netherlands, 2002.
20. Murakami, Y. Material defects as the basis of fatigue design. *Int. J. Fatigue* **2012**, *41*, 2–10. [[CrossRef](#)]
21. Garb, C.; Leitner, M.; Grün, F. Application of $\sqrt{\text{area}}$ -concept to assess fatigue strength of AlSi7Cu0.5Mg casted components. *Eng. Fract. Mech.* **2017**, *185*, 61–71. [[CrossRef](#)]
22. Leitner, M.; Garb, C.; Remes, H.; Stoschka, M. Microporosity and statistical size effect on the fatigue strength of cast aluminium alloys EN AC-45500 and 46200. *Mater. Sci. Eng. A* **2017**, *707*, 567–575. [[CrossRef](#)]
23. Garb, C.; Leitner, M.; Grün, F. Fatigue Strength Assessment of AlSi7Cu0.5Mg T6W Castings Supported by Computed Tomography Microporosity Analysis. *Procedia Eng.* **2016**, *160*, 53–60. [[CrossRef](#)]
24. DIN EN 515. *Aluminium and Aluminium Alloys-Wrought Products-Temper Designations*; Beuth Verlag: Berlin, Germany, 2017.
25. Sjölander, E.; Seifeddine, S. The heat treatment of Al-Si-Cu-Mg casting alloys. *J. Mater. Process. Technol.* **2010**, *210*, 1249–1259. [[CrossRef](#)]
26. Vandersluis, E.; Ravindran, C. Comparison of Measurement Methods for Secondary Dendrite Arm Spacing. *Metallogr. Microstruct. Anal.* **2017**, *6*, 89–94. [[CrossRef](#)]
27. Zhang, L.Y.; Jiang, Y.H.; Ma, Z.; Shan, S.F.; Jia, Y.Z.; Fan, C.Z.; Wang, W.K. Effect of cooling rate on solidified microstructure and mechanical properties of aluminium-A356 alloy. *J. Mater. Process. Technol.* **2008**, *207*, 107–111. [[CrossRef](#)]
28. DIN EN ISO 6892-1. *Metallic Materials-Tensile Testing-Part 1: Method of Test at Room Temperature*; Beuth Verlag: Berlin, Germany, 2016.
29. DIN EN ISO 6892-2. *Metallic Materials-Tensile Testing-Part 2: Method of Test At Elevated Temperature*; Beuth Verlag: Berlin, Germany, 2011.
30. Zhu, X.; Shyam, A.; Jones, J.; Mayer, H.; Lasecki, J.V.; Allison, J.E. Effects of microstructure and temperature on fatigue behavior of E319-T7 cast aluminum alloy in very long life cycles. *Int. J. Fatigue* **2006**, *28*, 1566–1571. [[CrossRef](#)]
31. Rincón, E.; López, H.F.; Cisneros, M.M.; Mancha, H.; Cisneros, M.A. Effect of temperature on the tensile properties of an as-cast aluminum alloy A319. *Mater. Sci. Eng. A* **2007**, *452-453*, 682–687. [[CrossRef](#)]
32. Zamani, M.; Seifeddine, S.; Jarfors, A.E. High temperature tensile deformation behavior and failure mechanisms of an Al-Si-Cu-Mg cast alloy—The microstructural scale effect. *Mater. Des.* **2015**, *86*, 361–370. [[CrossRef](#)]
33. Mohamed, A.; Samuel, F.H.; kahtani, S.A. Microstructure, tensile properties and fracture behavior of high temperature Al-Si-Mg-Cu cast alloys. *Mater. Sci. Eng. A* **2013**, *577*, 64–72. [[CrossRef](#)]

34. Khan, S.; Ourdjini, A.; Named, Q.S.; Alam Najafabadi, M.A.; Elliott, R. Hardness and mechanical property relationships in directionally solidified aluminium-silicon eutectic alloys with different silicon morphologies. *J. Mater. Sci.* **1993**, *28*, 5957–5962. [[CrossRef](#)]
35. Cahoon, J.R.; Broughton, W.H.; Kutzak, A.R. The determination of yield strength from hardness measurements. *Metall. Trans.* **1971**, *2*, 1979–1983. [[CrossRef](#)]
36. DIN EN ISO 6507. *Metallic Materials-Vickers Hardness Test-Part 1: Test Method*; Beuth Verlag: Berlin, Germany, 2018.
37. Tiryakioğlu, M.; Robinson, J.S.; Salazar-Guapuriche, M.A.; Zhao, Y.Y.; Eason, P.D. Hardness–strength relationships in the aluminum alloy 7010. *Mater. Sci. Eng. A* **2015**, *631*, 196–200. [[CrossRef](#)]
38. Rometsch, P.; Schaffer, G. An age hardening model for Al–7Si–Mg casting alloys. *Mater. Sci. Eng. A* **2002**, *325*, 424–434. [[CrossRef](#)]
39. Tiryakioğlu, M.; Campbell, J.; Staley, J.T. On macrohardness testing of Al–7 wt.% Si–Mg alloys: II. An evaluation of models for hardness–yield strength relationships. *Mater. Sci. Eng. A* **2003**, *361*, 240–248. [[CrossRef](#)]
40. Drouzy, M.; Jacob, S.; Richard, M. Interpretation of tensile results by means of quality index and probable Yield Strength-application to Al–Si7 Mg foundry alloys. *Int. Cast Met. J.* **1980**, *5*, 43–50.
41. ASTM International E 739. *Standard Practice for Statistical Analysis of Linear or Linearized Stress-Life (S-N) and Strain Life (E-N) Fatigue Data*; ASTM International: West Conshohocken, PA, USA, 1998.
42. Dengel, D.; Harig, H. Estimation of the fatigue limit by progressively-increasing load tests. *Fatigue Fract. Eng. Mater. Struct.* **1980**, *3*, 113–128. [[CrossRef](#)]
43. Dengel, D. Die arc sin \sqrt{P} -Transformation—Ein einfaches Verfahren zur grafischen und rechnerischen Auswertung geplanter Wöhlerversuche. *Materialwissenschaft und Werkstofftechnik* **1975**, *6*, 253–261. [[CrossRef](#)]
44. Leitner, H. Simulation des Ermüdungsverhaltens von Aluminiumgusslegierungen. Ph.D. Thesis, Montanuniversität Leoben, Leoben, Austria, 2001.
45. McKelvey, S.A.; Lee, Y.L.; Barkey, M.E. Stress-based uniaxial fatigue analysis using methods described in FKM-guideline. *J. Failure Anal. Prev.* **2012**, *12*, 445–484. [[CrossRef](#)]
46. Sonsino, C.M.; Dieterich, K. Einfluss der Porosität auf das Schwingfestigkeitsverhalten von Aluminium-Gusswerkstoffen. II. *Giessereiforschung* **1991**, *43*, 131–140.
47. Sonsino, C.M.; Dieterich, K. Einfluss der Porosität auf das Schwingfestigkeitsverhalten von Aluminium-Gusswerkstoffen. I. *Giessereiforschung* **1991**, *43*, 119–130.
48. Aigner, R.; Leitner, M.; Stoschka, M. Fatigue strength characterization of Al–Si cast material incorporating statistical size effect. *MATEC Web Conf.* **2018**, *165*, 14002. [[CrossRef](#)]
49. González, R.; Martínez, D.I.; González, J.A.; Talamantes, J.; Valtierra, S.; Colás, R. Experimental investigation for fatigue strength of a cast aluminium alloy. *Int. J. Fatigue* **2011**, *33*, 273–278. [[CrossRef](#)]
50. Tiryakioğlu, M. On the size distribution of fracture-initiating defects in Al- and Mg-alloy castings. *Mater. Sci. Eng. A* **2008**, *476*, 174–177. [[CrossRef](#)]
51. Beretta, S.; Murakami, Y. Statistical analysis of defects for fatigue strength prediction and quality control of materials. *Fatigue Fract. Eng. Mater. Struct.* **1998**, *21*, 1049–1065. [[CrossRef](#)]
52. Souza, D.; Menegalli, F.C. Image analysis: Statistical study of particle size distribution and shape characterization. *Powder Technol.* **2011**, *214*, 57–63. [[CrossRef](#)]
53. Garb, C.; Leitner, M.; Tauscher, M.; Weidt, M.; Brunner, R. Statistical analysis of micropore size distributions in Al–Si castings evaluated by X-ray computed tomography. *Int. J. Mater. Res.* **2018**, *109*, 889–899. [[CrossRef](#)]
54. Makhlof, K.; Jones, J. Near-threshold fatigue crack growth behaviour of a ferritic stainless steel at elevated temperatures. *Int. J. Fatigue* **1992**, *14*, 97–104. [[CrossRef](#)]
55. Alvarez Holston, A.M.; Stjärnsäter, J. On the effect of temperature on the threshold stress intensity factor of delayed hydride cracking in light water reactor fuel cladding. *Nuclear Eng. Technol.* **2017**, *49*, 663–667. [[CrossRef](#)]
56. Ritchie, R.O. Near-threshold fatigue-crack propagation in steels. *Int. Met. Res.* **2013**, *24*, 205–230. [[CrossRef](#)]
57. Irwin, G.R. Analysis of stresses and strains near the end of a crack traversing a plate. *J. Appl. Mech.* **1957**, *24*, 361–364.
58. Pippin, R.; Hohenwarther, A. Fatigue crack closure: A review of the physical phenomena. *Fatigue Fract. Eng. Mater. Struct.* **2017**, *40*, 471–495. [[CrossRef](#)]

59. McClung, R.C. Crack closure and plastic zone sizes in fatigue. *Fatigue Fract. Eng. Mater. Struct.* **1991**, *14*, 455–468. [[CrossRef](#)]
60. Hou, C.; Charng, J. Estimation of plasticity-induced crack closure in a pre-existing plastic zone. *Int. J. Fatigue* **1996**, *18*, 463–474. [[CrossRef](#)]
61. Zhang, W.; Liu, Y. Plastic zone size estimation under cyclic loadings using in situ optical microscopy fatigue testing. *Fatigue Fract. Eng. Mater. Struct.* **2011**, *34*, 717–727. [[CrossRef](#)]



© 2018 by the authors. Licensee MDPI, Basel, Switzerland. This article is an open access article distributed under the terms and conditions of the Creative Commons Attribution (CC BY) license (<http://creativecommons.org/licenses/by/4.0/>).